Robust room temperature valley Hall effect of interlayer excitons

Huang, Zumeng; Liu, Yuanda; Dini, Kévin; Tan, Qinghai; Liu, Zhuojun; Fang, Hanlin; Liu, Jin; Liew, Timothy; Gao, Weibo

2020

Huang, Z., Liu, Y., Dini, K., Tan, Q., Liu, Z., Fang, H., Liu, J., Liew, T. & Gao, W. (2020). Robust room temperature valley Hall effect of interlayer excitons. Nano Letters, 20(2), 1345-1351. https://dx.doi.org/10.1021/acs.nanolett.9b04836

https://hdl.handle.net/10356/147882

https://doi.org/10.1021/acs.nanolett.9b04836

Robust room temperature valley Hall effect of interlayer excitons

Zumeng Huang,[†] Yuanda Liu,[†] Kévin Dini,[†] Qinghai Tan,[†] Zhuojun Liu,[‡] Hanlin Fang,[‡] Jin Liu,[‡] Timothy Liew[†] and Weibo Gao[,†,||]*

[†]Division of Physics and Applied Physics, School of Physical and Mathematical Sciences, Nanyang Technological University, Singapore

[‡]State Key Laboratory of Optoelectronic Materials and Technologies, School of Physics, Sun Yat-sen University, Guangzhou 510275, China

[||]The Photonics Institute and Centre for Disruptive Photonic Technologies, Nanyang Technological University, Singapore

ABSTRACT

The Berry curvature in the band structure of transition metal dichalcogenides (TMDs) introduces a valley-dependent effective magnetic field, which induces the valley Hall effect (VHE). Similar to the ordinary Hall effect, the VHE spatially separates carriers or excitons, depending on their valley index, and accumulates them at opposite sample edges. The VHE can play a key role in valleytronic devices, but previous observations of the VHE have been limited to cryogenic temperatures. Here, we report a demonstration of the VHE of interlayer excitons in a MoS_2/WSe_2

heterostructure at room temperature. We monitored the in-plane propagation of interlayer excitons through photoluminescence mapping and observed their spatial separation into two opposite transverse directions that depended on the valley index of the excitons. Our theoretical simulations reproduced the salient features of these observations. Our demonstration of the robust interlayer exciton VHE at room temperature, enabled by their intrinsically long lifetimes, will open up realistic possibilities for the development of opto-valleytronic devices based on TMD heterostructures.

KEYWORDS

TMD heterostructures; interlayer excitons; valley hall effect; room temperature; valley polarization

TEXT

Introduction

In monolayer transition metal dichalcogenide (TMD) materials, two valleys, located at inequivalent corners of the hexagonal first Brillouin zone, have the same energy but opposite Berry curvatures.[1-4] These Berry curvatures serve as effective magnetic fields,[5] which exert an effective force on accelerating carriers to deflect their transport current.[6] The direction of this force, however, is valley dependent because of the opposite signs of the Berry curvatures, resulting in valley-dependent spatial separation of carriers. This so-called valley Hall effect (VHE), analogous to the spin-dependent spatial separation in the spin Hall effect,[7] has been observed for electrons in a MoS_2 transistor.[8] Furthermore, the excitonic version of the VHE has been theoretically proposed [9-13] and experimentally demonstrated in monolayer MoS_2[14] with a larger Hall angle. The

observation of the excitonic VHE is particularly important for developing novel valley-dependent optoelectronic devices utilizing TMD materials.

However, as has been shown in time- and polarization-dependent photoluminescence (PL) measurements, excitons in monolayer TMDs possess short valley lifetimes, typically in the picosecond range. In addition, the valley depolarization process gets even faster with increasing temperature, and the VHE has remained to be a low-temperature phenomenon. The strong electron-hole exchange interactions are believed to be responsible for the rapid valley depolarization of excitons. The valley lifetime of excitons can be significantly extended by using TMD van der Waals heterostructures.[15, 16] In a TMD heterostructure with type-II alignment, electrons and holes stay in different layers. The formation time of such interlayer (or indirect) excitons is very short, typically on the order of 50 fs,[17, 18] and the binding energies are still considerable despite the charge separation.[19] The electron-hole wavefunction overlap is heavily reduced, which not only leads to a long exciton lifetime due to the reduced recombination probability but also a long valley lifetime due to the reduced electron-hole exchange interaction.[1, 16] Therefore, interlayer excitons are ideal candidates for serving as robust carriers of valley information.[20, 21]

Here, we report on the first observation of the VHE of interlayer excitons in MoS_2/WSe_2 heterostructures. Due to the type-II band alignment, electrons and holes reside in MoS_2 and WSe_2, respectively, forming robust interlayer excitons.[17, 22, 23] We used spatially resolved polarization-dependent PL spectroscopy to map the intensity and polarization of PL emission from interlayer excitons and observed that they are spatially separated into two opposite transverse directions, depending on the valley index. We directly demonstrated a long (~ 1 ns) valley lifetime through time-resolved PL measurements, and finite valley polarization persisted up to room temperature.

Consequently, the interlayer exciton VHE was robust, observed in different samples under various conditions of temperature, excitation wavelength, and excitation polarization. To enhance the VHE we use a unique suspended slab geometry where strain and consequently a strong potential gradient are expected. These observations demonstrate that interlayer excitons in TMD heterostructures are promising for implementing valley-dependent properties in optoelectronic devices.

Results

Figure 1a shows a schematic energy-level diagram for interlayer excitons in a MoS_2/WSe_2 heterostructure with a stacking angle near zero degree. An interlayer exciton consists of an electron in the MoS_2 layer and a hole in the WSe_2 layer; It can radiatively recombine and emit a photon. Because of the lack of inversion symmetry, the K and K' points are inequivalent in momentum space although their energies are degenerate. Due to spin-orbit coupling, different valleys have opposite circular polarization selection rules (Figure 1a),[1, 24, 25] which allows us to detect excitons in different valleys with their exclusive optical helicity (σ^+ and σ^-). We characterized the MoS_2-WSe_2 monolayers and heterostructures using PL measurements. Their spectrum is shown in Figure 1b. Intralayer excitons in MoS_2 (WSe_2) show a peak at ~675 nm (~750 nm), while interlayer excitons in the heterostructure area show a peak at ~1130 nm. We fabricated several samples, and they all corroborate this result (see Supplementary Section A). Note that the peak wavelength (1130 nm) is consistent with the previous reports for interlayer excitons associated with the K−K transition measured through scanning tunneling microscopy[23] but is different from those reports for interlayer excitons associated with the K− Γ transition,[26, 27] which have emission around 800 nm.

We also investigated the lifetime and valley polarization of the interlayer exciton emission peak at both cryogenic and room temperatures (Figure 1 c and d). An ultralong lifetime (~ 1 ns) was observed, confirming its interlayer exciton origin. Furthermore, by excited with a CW laser at 726 nm and only detected emission from interlayer exciton recombination using long pass filters, we collect the σ^+ and σ^- polarized PL intensity data, and calculated the degree of polarization (DOP) as $\left(I_{\sigma^+} - I_{\sigma^-}\right)/\left(I_{\sigma^+} + I_{\sigma^-}\right)$, where I_{σ^+} and I_{σ^-} are the average PL intensity for σ^+ and σ^- emission. The absolute value of DOP for both valleys were about 30% at the lowest temperature, gradually decreased with increasing temperature, and became ~6% at room temperature.

Figure 2a shows an optical microscope image of a representative device. The WSe_2 and MoS_2 monolayers were mechanically exfoliated from bulk single crystals onto polydimethylsiloxane stamps. Then they were stacked onto a silicon-on-insulator wafer with a 220 nm thick silicon film on a 2 μm sacrificial silicon dioxide layer (see the Methods section for more details). Etching chemicals are then injected through the holes of the silicon layer to create an empty etched area below the system. As shown in Figure 2b, the silicon and the heterobilayer are therefore suspended which results in the appearance of strain at the edges of the slab. This strain, as described below, induces a potential required for the appearance of the VHE. Furthermore, excitons in different valleys are expected to exhibit valley-contrasting transverse motion due to the opposite signs of their Berry curvatures, which were illustrated in Figure 2c.

The experimental setup used for polarization-dependent PL mapping is schematically shown in Figure 3a, and a detailed description can be found in the Methods section. In order to measure exciton transport, we fixed the excitation laser spot on the sample and then scanned the detection spot. Note that this scheme is different from normal PL mapping methods as used in

Supplementary Figures S1 and S3, for which the excitation and emission spot always overlapped with each other in a confocal microscope.

To characterize our setup, we first scan the emission pattern for the silicon PL from a heavily doped SiO_2-Si wafer, for which the shape should be centrosymmetric. As expected, the intensity distribution shows a Gaussian shape around the center of the excitation beam (Figure 2b). Next, we scan the emission pattern for interlayer exciton PL. Figure 3c shows a measured diagram which significantly distorts from the Gaussian shape. Clear peaks appear, and through comparison with sample images, we determined that the sidebands appeared at suspended slab edges. Similar patterns were observed in different samples that did not have the periodic holes but had strain at the edges (shown in Supplementary Figure S8b).

Given the clearly detectable exciton transport, we then performed polarization-dependent PL mapping experiments. We used a linearly polarized excitation beam to make sure that both valleys are equally populated and monitored right (σ^+) and left (σ^-) circularly polarized PL. With these data, we calculated the DOP map as shown in Figure 4a. After exciton propagating toward the sample edges (in directions indicated by the arrows), separation occurs between negative (blue) and positive (red) DOP regions. To see it more clearly, Figures 4b and 4c show line cuts of the PL intensity and DOP along the green dashed line in Figure 4a. The σ^+ and σ^- emission components are separated along the transverse (y) direction, with the corresponding DOP showing different signs. The PL intensity and DOP in another direction (yellow line) are shown in Figures 4d and 4e, which have similar behavior. From Figures 4b and 4d, we determined the distance between the separated intensity peaks (σ^+ and σ^-) to be 0.41 ± 0.02 μm and 0.33 ± 0.07 μm for the green and yellow line cuts, respectively.

While the previous observation of the exciton VHE in monolayer MoS_2 was possible only at low temperatures, we can observe the interlayer exciton VHE even at room temperature, as shown in Figure 5. The first reason for that as described previously is the robustness of the interlayer excitons, giving them a long exciton and valley lifetime even at room temperature. The second one is that in previous experiments the gradient of potential was due to a gradient of temperature [14]. Here we design the system such that the existence of the gradient of potential is not temperature dependent. Clear separation between the σ^+ and σ^- components, similar to the low-temperature data in Figure 4, can be seen even though the contrast is smaller. The separation between the peaks is 0.30 ± 0.02 μm. We also moved the excitation spot to a different location on the samples (shown in Figure 5d-f). The results observed are similar to what is observed when the spot is not moved.

In order to understand the observed polarization-dependent emission patterns, we developed a theoretical model and performed simulations. As the excitons in different valleys carry opposite Berry curvatures, when encountering a potential gradient, they will gain a valley-dependent transverse velocity. A way to describe such an effect is to introduce the following term in the exciton velocity:[6]

$$\vec{v}_{\Omega} = \vec{\nabla} V(r) \times \vec{\Omega}$$

where $\vec{\Omega}$ is the Berry curvature and $V(r)$ is the potential.

For simulating the dynamics of interlayer excitons, we iteratively solved the equation of motion associated with the exciton ballistic motion and then calculated the average trajectory of many excitons, which are all assumed to originate from the pump spot center with uniformly distributed

initial propagation directions and a Bose-Einstein distribution of initial energies (corresponding to different initial speeds).

Since the distance between the center of the pump spot and the edge depends on the direction, the intensity of the exciton will be larger for four particular directions. Therefore, for a centered pump we expect to obtain five high intensity spots: the central pump and four recombination spots on the edge. When reaching an edge of the system, the excitons encounter a potential barrier due to strain induced by bending of the silicon suspended layer. The localized pump laser can induce a temperature gradient from the center of the sample to the edge.[14] However, this gradient seems to be very small and therefore we choose to not include it in the simulations.

Introducing the edge potential in the equation of motion along with the Berry induced velocity, we obtain the DOP in the vicinity of the edges of the sample; see Figure 6. The DOP strongly depends on the value of the Berry curvature as well as the intensity and shape of the potential. We assumed the potential to be half a Gaussian near the edge with a maximum amplitude of 200 meV and a half width of 0.5 μm. Similar to TMD monolayers, here we have taken the Berry curvature to be 15 Å^2. With these parameters, we obtained the DOP and intensity distributions shown in Figure 6, which exhibit reasonable qualitative agreement with the experimental patterns. The quantitative difference between the intensity distributions in the model and the experiment can be attributed to extra energy relaxation processes omitted in the model.

To further explore the robustness of the observed interlayer-exciton VHE, we examined the PL emission patterns under different conditions. First, we used different excitation polarizations (Figures S5 and S6). After rotating the polarization direction of the linearly polarized excitation beam by 90 degrees, we obtained essentially the same results. Next, we demonstrated the VHE by

using different excitation laser wavelengths (see Figure S7). Finally, in order to confirm that the origin of the potential is strain, we construct new samples, i.e., we stack directly the heterobilayer/h-BN on the SOI with rectangular holes at surface, which creates the aforementioned strain. As expected, the VHE is still present (Figure S8).

Discussion

In summary, we report the first observation of the room temperature valley Hall effect using interlayer excitons in MoS_2/WSe_2 heterostructures. The robustness of exciton transport at room temperature comes from the much longer exciton and valley lifetimes as compared to that of intralayer excitons. Future work may include using electric field to control the transport of interlayer excitons since they possess an out of plane dipole with electron and hole separated in different layers.[28-30] Other fundamental questions include how the exciton repulsive interaction induced valley-polarized exciton gas and valley Hall effect affect each other; and how the VHE plays a role in exciton superfluidics in TMD heterostructures.[31] We note that valley separation has been achieved with the assistance of well-designed metasurfaces[32] and subwavelength asymmetric groove arrays.[33] Our demonstration of the control of valley information might open new possibilities of opto-electronics and valleytronics applications for interlayer excitons.

FIGURES

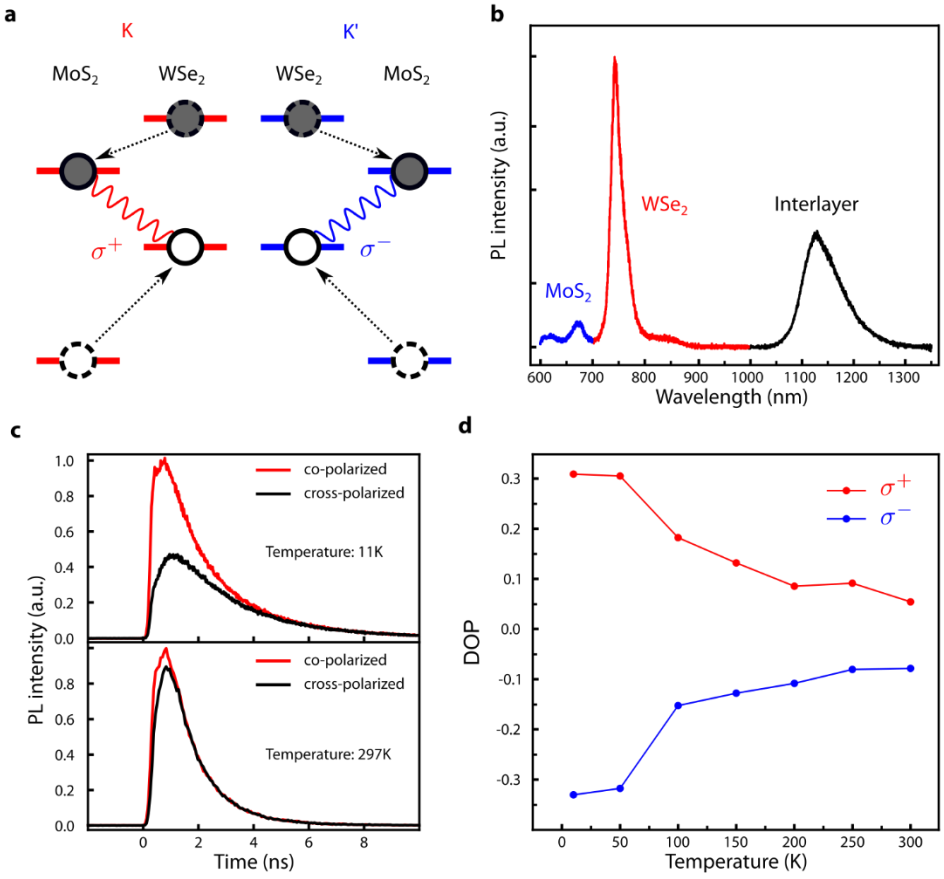

Figure 1. Valley polarization of the interlayer exciton. (a) Interlayer exciton in different valleys. Electrons (grey dots) will hop to MoS_2 with a lower energy in the conduction band. Holes (empty dots) will hop to the valence band of WSe_2. The combination of electrons and holes emits photons with optical helicity. σ^+ (σ^-) circularly polarized light couples to the K (K') valley. (b) PL from intralayer and interlayer excitons. The wavelength of interlayer exciton emission is well separated from that in monolayer MoS_2 and WSe_2, making sure that we can detect interlayer exciton emission exclusively by using a long pass filter. (c) Time-resolved PL measurement for co-polarized and cross-polarized situation in low temperature (up) and room temperature (down). (d) DOP as a function of temperature for σ^+ and σ^- excitation. The valley polarization starts from around 30% and reduces to about 6% as the temperature goes higher from cryogenic temperature to room temperature. The error bar is smaller than the size of the dot.

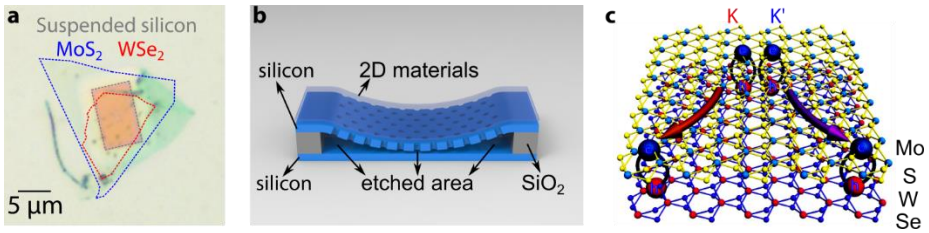

Figure 2. Concept of interlayer exciton valley hall effect. (a) Microscope image for our sample. The red dashed line represents monolayer WSe_2. The blue dashed line represents monolayer MoS_2. WSe_2 and MoS_2 are stacked on a silicon-on-insulator (SOI) substrate by dry transfer. In the middle of the substrate, a silicon suspended slab is fabricated in rectangular shape. (b) Schematic illustration of the silicon suspended slab. The suspended silicon layer is made of SOI material with a nominal 220 nm thick silicon layer on 2 μm buried oxide. It will bend due to gravity and create strain where the maximum is at the edge. Blue layer, silicon; gray layer, SiO_2; top transparent layer: 2D materials. (c) Side view of heterostructures with MoS_2 and WSe_2 monolayers. Under their Berry curvature and the external strain, interlayer excitons formed by electrons (e) and holes (h) will traverse to different directions according to their valleys (K and K').

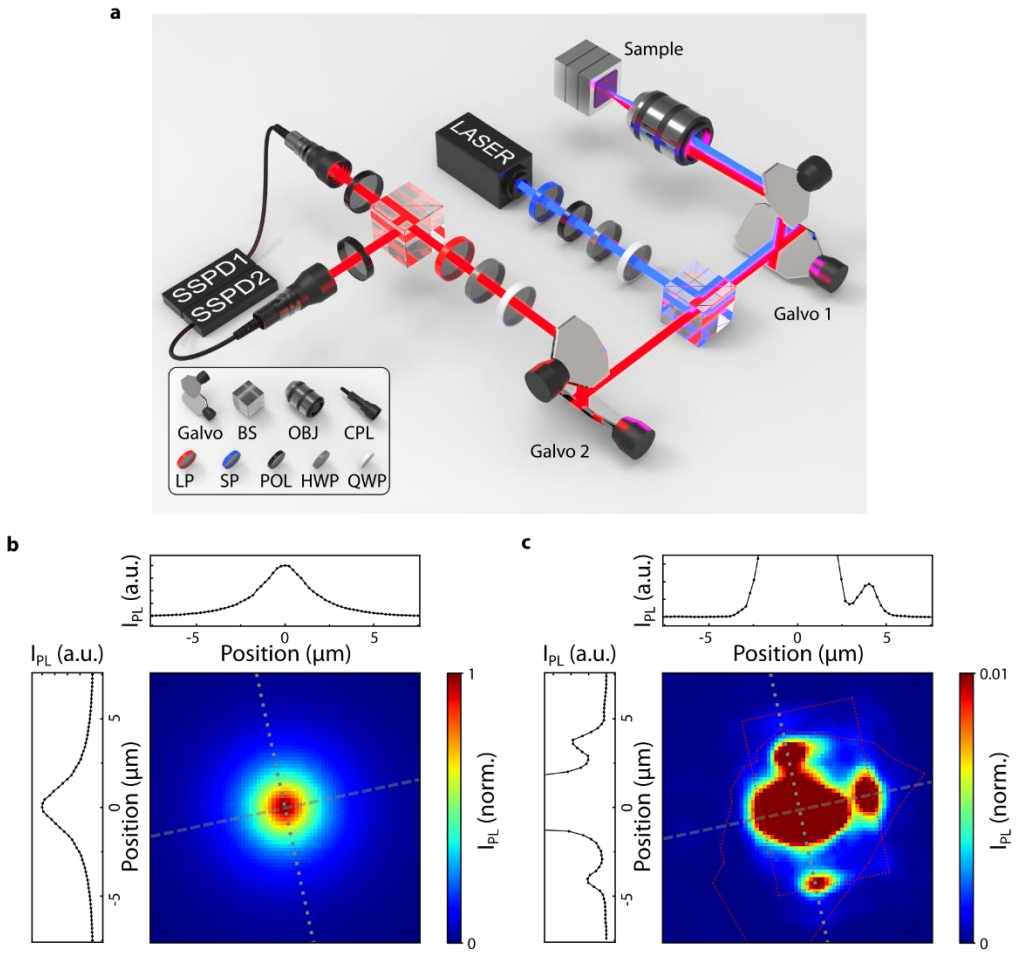

Figure 3. Experimental setup and detection of exciton transport. (a) Experimental setup. The sample is in a closed-cycle cryostat with variable temperature. A laser with controllable polarization is sent to the sample through a scanning galvo mirror set. PL is sent to the superconducting single photon detector (SSPD). The Galvo in the PL collection arm is used to implement PL mappings (See detail in the Method). BS, beam splitter; OBJ, objective lens; CPL, coupler; LP, long pass filter; SP, short pass filter; POL, polarizer; HWP, half wave plate; QWP, quarter wave plate. (b) The emission pattern for silicon PL. By scanning the Galvo 2 mirror set, we are able to detect the emission spatial profiles. As expected, the emission spot shows a Gaussian shape. The intensity as a function of position is shown on top for the horizontal linecut. The one for the vertical linecut is shown on the left. (c) Emission pattern for interlayer exciton PL. In stark

contrast, here the emission shows a non-Gaussian profile. To see the profile more clearly, here we set the maximum intensity as one percent of the observed peak intensity. From the linecuts, we can see photon sidebands in both the horizontal and vertical directions. These sidebands come from the exciton transport over a sizable distance. The edges of the heterostructures and suspended rectangle substrate are shown with the red dashed line (the same for all other figures).

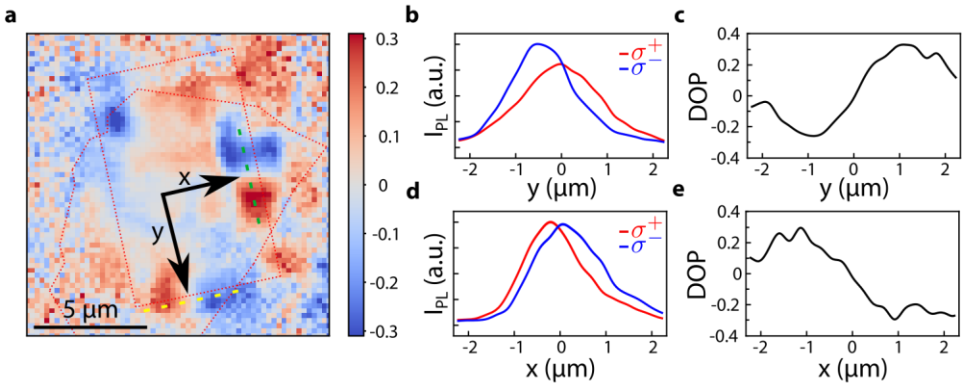

Figure 4. Experimental demonstration of exciton valley Hall effect at cryo-temperature. (a) Degree of polarization. The origin of the x and y axes is at the excitation spot. (b) PL intensity with different polarization following the green linecut in (a). A separation of the intensity peak can be seen in the y direction, perpendicular to the exciton transport in the x direction. (c) Degree of polarization (DOP) as calculated from (b). (d) PL intensity with different polarization following the yellow linecut in (a). Separation of emission intensity peak and therefore different exciton movement in the transverse direction can be seen as well. (e) DOP as calculated from (d).

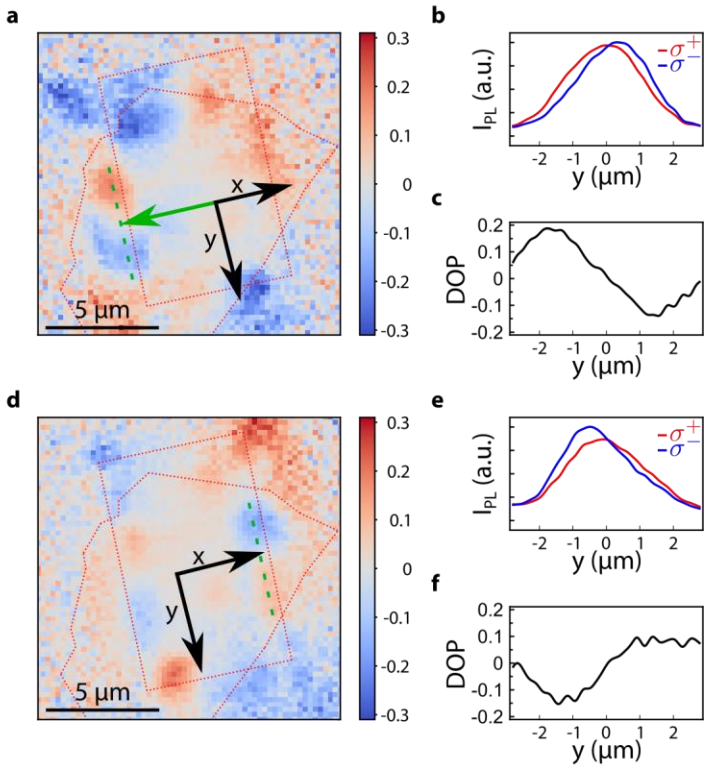

Figure 5. Room-temperature valley Hall effect. (a) Degree of polarization at room temperature. The green arrow represents the exciton transport direction from the excitation spot. Intensity (b) and DOP (c) following the dashed green linecut in (a). (d) Degree of polarization for another excitation spot. Intensity (e) and DOP (f) following the dashed green linecut in (d). The intensity peak separation is reversed in (b) and (e), due to the reversal of the dominant exciton transport direction.

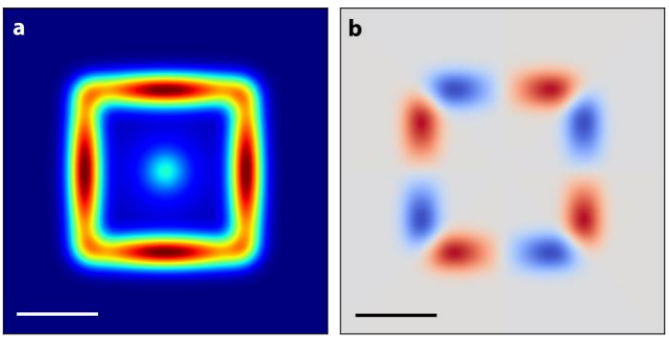

Figure 6. Degree of polarization and intensity distribution in the simulation. (a) Simulated total emission from a square shaped edge potential area. (b) Simulated DOP distribution. The σ^+ and σ^- emission will split along the edge because of VHE and build up a DOP difference. The scale bar is 5 μm.

ASSOCIATED CONTENT

Supporting Information.

The following files are available free of charge.

MoS_2/WSe_2 interlayer excitons, the influence of the SOI slab, setup characterizations, excitation polarization dependence, excitation wavelength dependence, VHE experiment on sample II with etched structure on substrate and Figures S1-S8 (PDF)

AUTHOR INFORMATION

Corresponding Author

* Email: wbgao@ntu.edu.sg

Author Contributions

W.G., T.L. and J.L. supervised the project. Z.H. conceived, performed the experiment and analyzed the data. Y.L., Q.T. and H.F. fabricated the samples. K.D. conceived and carried out modeling. The manuscript was written through contributions of all authors.

ACKNOWLEDGMENT

We acknowledge the support from the Singapore National Research Foundation (NRF-NRFF2015-03) and its Competitive Research Program (CRP Award No. NRF-CRP21-2018-0007),

Singapore Ministry of Education (MOE2016-T2-2-077, MOE2016-T2-1-163, MOE2016-T3-1-006 (S)), A*Star QTE programme.

REFERENCES

1. Xiao, D.; Liu, G.-B.; Feng, W.; Xu, X.; Yao, W. *Phys. Rev. Lett.* **2012,** 108, (19), 196802.
2. Cao, T.; Wang, G.; Han, W.; Ye, H.; Zhu, C.; Shi, J.; Niu, Q.; Tan, P.; Wang, E.; Liu, B. *Nat. Commun.* **2012,** 3, 887.
3. Zeng, H.; Dai, J.; Yao, W.; Xiao, D.; Cui, X. *Nat. Nanotechnol.* **2012,** 7, (8), 490.
4. Jones, A. M.; Yu, H.; Ghimire, N. J.; Wu, S.; Aivazian, G.; Ross, J. S.; Zhao, B.; Yan, J.; Mandrus, D. G.; Xiao, D. *Nat. Nanotechnol.* **2013,** 8, (9), 634.
5. Srivastava, A.; Sidler, M.; Allain, A. V.; Lembke, D. S.; Kis, A.; Imamoğlu, A. *Nat. Phys* **2015,** 11, (2), 141.
6. Xiao, D.; Chang, M.-C.; Niu, Q. *Rev. Mod. Phys.* **2010,** 82, (3), 1959.
7. Sinova, J.; Valenzuela, S. O.; Wunderlich, J.; Back, C.; Jungwirth, T. *Rev. Mod. Phys.* **2015,** 87, (4), 1213.
8. Mak, K. F.; McGill, K. L.; Park, J.; McEuen, P. L. *Science* **2014,** 344, (6191), 1489-1492.
9. Yao, W.; Niu, Q. *Phys. Rev. Lett.* **2008,** 101, (10), 106401.
10. Kuga, S.-i.; Murakami, S.; Nagaosa, N. *Phys. Rev. B* **2008,** 78, (20), 205201.
11. Yu, H.; Liu, G.-B.; Gong, P.; Xu, X.; Yao, W. *Nat. Commun.* **2014,** 5, 3876.
12. Li, Y.-M.; Li, J.; Shi, L.-K.; Zhang, D.; Yang, W.; Chang, K. *Phys. Rev. Lett.* **2015,** 115, (16), 166804.
13. Yu, T.; Wu, M. *Phys. Rev. B* **2016,** 93, (4), 045414.
14. Onga, M.; Zhang, Y.; Ideue, T.; Iwasa, Y. *Nat. Mater.* **2017,** 16, (12), 1193.
15. Rivera, P.; Seyler, K. L.; Yu, H.; Schaibley, J. R.; Yan, J.; Mandrus, D. G.; Yao, W.; Xu, X. *Science* **2016,** 351, (6274), 688-691.
16. Jiang, C.; Xu, W.; Rasmita, A.; Huang, Z.; Li, K.; Xiong, Q.; Gao, W.-b. *Nat. Commun.* **2018,** 9, (1), 753.
17. Hong, X.; Kim, J.; Shi, S.-F.; Zhang, Y.; Jin, C.; Sun, Y.; Tongay, S.; Wu, J.; Zhang, Y.; Wang, F. *Nat. Nanotechnol.* **2014,** 9, (9), 682.
18. Zheng, W.; Zheng, B.; Jiang, Y.; Yan, C.; Chen, S.; Liu, Y.; Sun, X.; Zhu, C.; Qi, Z.; Yang, T. *Nano letters* **2019**.
19. Rivera, P.; Schaibley, J. R.; Jones, A. M.; Ross, J. S.; Wu, S.; Aivazian, G.; Klement, P.; Seyler, K.; Clark, G.; Ghimire, N. J. *Nat. Commun.* **2015,** 6, 6242.
20. Jin, C.; Kim, J.; Utama, M. I. B.; Regan, E. C.; Kleemann, H.; Cai, H.; Shen, Y.; Shinner, M. J.; Sengupta, A.; Watanabe, K. *Science* **2018,** 360, (6391), 893-896.
21. Cheng, R.; Wang, F.; Yin, L.; Wang, Z.; Wen, Y.; Shifa, T. A.; He, J. *Nature Electronics* **2018,** 1, (6), 356.
22. Pant, A.; Mutlu, Z.; Wickramaratne, D.; Cai, H.; Lake, R. K.; Ozkan, C.; Tongay, S. *Nanoscale* **2016,** 8, (7), 3870-3887.

23. Chiu, M.-H.; Zhang, C.; Shiu, H.-W.; Chuu, C.-P.; Chen, C.-H.; Chang, C.-Y. S.; Chen, C.-H.; Chou, M.-Y.; Shih, C.-K.; Li, L.-J. *Nat. Commun.* **2015,** 6, 7666.
24. Schaibley, J. R.; Yu, H.; Clark, G.; Rivera, P.; Ross, J. S.; Seyler, K. L.; Yao, W.; Xu, X. *Nature Reviews Materials* **2016,** 1, (11), 16055.
25. Mak, K. F.; Xiao, D.; Shan, J. *Nat. Photon.* **2018,** 12, (8), 451.
26. Kunstmann, J.; Mooshammer, F.; Nagler, P.; Chaves, A.; Stein, F.; Paradiso, N.; Plechinger, G.; Strunk, C.; Schüller, C.; Seifert, G. *Nat. Phys* **2018,** 14, (8), 801.
27. Fang, H.; Battaglia, C.; Carraro, C.; Nemsak, S.; Ozdol, B.; Kang, J. S.; Bechtel, H. A.; Desai, S. B.; Kronast, F.; Unal, A. A. *Proc. Natl. Acad. Sci. U. S. A.* **2014,** 111, (17), 6198-6202.
28. Unuchek, D.; Ciarrocchi, A.; Avsar, A.; Watanabe, K.; Taniguchi, T.; Kis, A. *Nature* **2018,** 560, (7718), 340.
29. High, A. A.; Novitskaya, E. E.; Butov, L. V.; Hanson, M.; Gossard, A. C. *Science* **2008,** 321, (5886), 229-231.
30. Grosso, G.; Graves, J.; Hammack, A.; High, A.; Butov, L.; Hanson, M.; Gossard, A. *Nat. Photon.* **2009,** 3, (10), 577.
31. Fogler, M.; Butov, L.; Novoselov, K. *Nat. Commun.* **2014,** 5, 4555.
32. Tran, K.; Moody, G.; Wu, F.; Lu, X.; Choi, J.; Kim, K.; Rai, A.; Sanchez, D. A.; Quan, J.; Singh, A. *Nature* **2019,** 567, (7746), 71.
33. Sun, L.; Wang, C.-Y.; Krasnok, A.; Choi, J.; Shi, J.; Gomez-Diaz, J. S.; Zepeda, A.; Gwo, S.; Shih, C.-K.; Alù, A. *Nat. Photon.* **2019,** 13, (3), 180.